

The accumulated persistence function, a new useful functional summary statistic for topological data analysis, with a view to brain artery trees and spatial point process applications

Christophe A.N. Biscio* and Jesper Møller*

September 29, 2018

Abstract: A persistent diagram is a multiset of points in the plane describing the persistence of topological features of a compact set when a scale parameter varies. Since statistical methods are difficult to apply directly on persistence diagrams, various alternative functional summary statistics have been suggested, but either they do not contain the full information of the persistence diagram or they are two-dimensional functions. This paper suggests a new functional summary statistic that is one-dimensional and hence easier to handle, and which under mild conditions contains the full information of the persistence diagram. Its usefulness is illustrated in various statistical settings concerned with point clouds and brain artery trees.

Keywords: clustering, confidence region, extreme rank envelope, functional boxplot, persistent homology, supervised classification, two-sample test.

1 Introduction

1.1 Background and objective

Persistence homology is an algebraic method for measuring the persistence of k -dimensional topological features of shapes and of functions, i.e. their connected components if $k = 0$ and their k -dimensional holes otherwise (loops if $d = 2$ and voids if $d = 3$). For the technical definition of persistence in terms of homology groups and filtrations of simplicial complexes, see Fasy *et al.* (2014) and the references therein. For Examples 1-10 in the present paper, it is only relevant to let $k = 0$ or $k = 1$.

Often a family of increasing or decreasing compact sets $\{C_t\}_{t \geq 0}$ in \mathbb{R}^d , where $t \geq 0$ has

*Department of Mathematical Sciences, Aalborg University, Denmark.

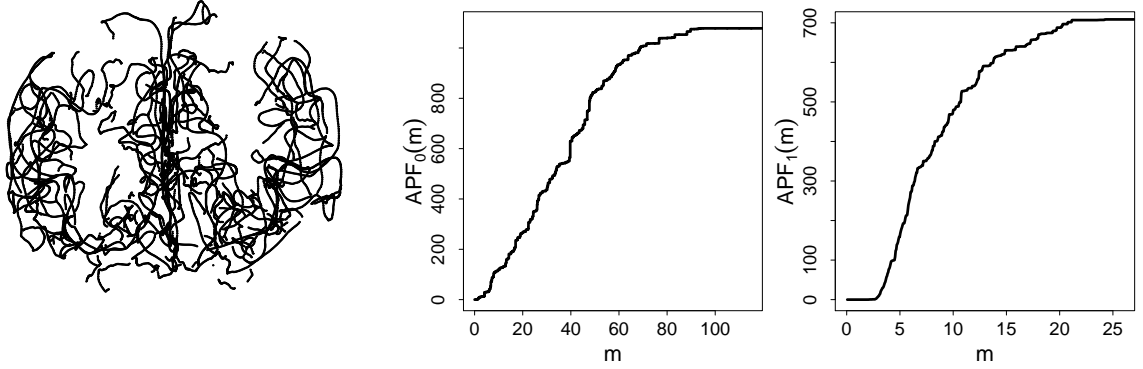


Figure 1: A brain artery tree (left panel), its corresponding APF_0 (middle panel) obtained from the sub-level set of the height function, and its corresponding APF_1 (right panel) obtained from the sub-level set of the distance function.

an interpretation as time or as a scale parameter, is used to describe the persistence. A simple example considered in this paper is a brain artery tree $B \subset \mathbb{R}^3$, see the left panel of Figure 1. Following Bendich *et al.* (2016), if $k = 0$, let $C_t = \{(x, y, z) \in B : z \leq t\}$ be a sub-level set of the height function for the tree; we refer to $\{C_t\}_{t \geq 0}$ as a Morse filtration. Consider the connected components of C_t as t increases: New components may appear (the case of births) or existing components may disappear (the case of deaths); in case two or more components emerge, only the oldest one survives; if there are two or more which are oldest, then we select one of them uniformly at random. The lifetime given by the difference between a corresponding birth and death is then the persistence of one or more connected components. Further details are given in Section 2.2, including the case $k = 1$ where C_t is defined as a sub-level set of the distance function to 3000 points on the tree.

Technically speaking, for each dimension $k = 0, 1, \dots$ and an index $i = 1, 2, \dots$, we may have a number c_i of homology classes born at scale b_i and dying at scale d_i , and their persistence is given by the lifetime $l_i = d_i - b_i$. A popular graphical representation of the persistence of the k -dimensional topological features is the *persistence diagram* given by the multiset PD_k of the points (b_i, d_i) with multiplicities c_i . For example, in case of the Morse filtration described above, the persistence diagram specifies the connected component evolution of the threshold sets of the height function, and c_i is the number of connected components with birth and death times (b_i, c_i) . In the majority of applications of persistence homology, including the analysis in Bendich *et al.* (2016) of brain artery trees, long lifetimes are of main interest whereas short lifetimes are considered as topological noise. Short lifetimes are of interest in the study of complex structures such as branch polymers and fractals, see MacPherson and Schweinhart (2012); and for brain artery trees Bendich *et al.* (2016) noticed in one case that "not-particularly-high persistence have the most distinguishing power in our specific application". In Section 3.2-5.3 we demonstrate that short lifetimes will also be of key interest in many situations, including when analysing the brain artery trees dataset from Bendich *et al.* (2016).

Chazal *et al.* (2013) and Chen *et al.* (2015) note that it is difficult to apply statistical methodology to random persistent diagrams. Alternative functional summary statistics have been suggested: Bubenik (2015) introduces a sequence of one-dimensional functions called the persistent landscape, where his first function is denoted λ_1 and is considered to be of main interest, since it provides a measure of the dominant topological features, i.e. the longest lifetimes; therefore we call λ_1 the dominant function. Chazal *et al.* (2013) introduce the silhouette which is a weighted average of the functions of the persistent landscape, where the weights control whether the focus is on topological features with long or short lifetimes. Moreover, Chen *et al.* (2015) consider a kernel estimate of the intensity function for the persistent diagram viewed as a point pattern. The dominant function, the silhouette, and the intensity estimate are one-dimensional functions and hence easier to handle than the persistence diagram, however, they provide selected and not full information about the persistence diagram. In Section 1.2, we introduce another one-dimensional functional summary statistic called the accumulative persistence function and discuss its advantages and how it differs from the existing functional summary statistics.

1.2 The accumulated persistence function

For simplicity and specificity, for each dimension k , we always assume that the persistence diagram $PD_k = \{(b_1, d_1, c_1), \dots, (b_n, d_n, c_n)\}$ is such that $n < \infty$ and $0 \leq b_i < d_i < \infty$ for $i = 1, \dots, n$. This assumption will be satisfied in the settings (i)-(ii) described in Section 2.1 and in our Examples 1, 2, 3, 5, 7, 9, and 10 with probability one (strictly speaking, in the settings (i)-(ii) and when $k = 0$, there is an infinite lifetime which just represents \mathbb{R}^2 , but we ignore this infinite lifetime since it is not informative). We call $m_i = (b_i + d_i)/2$ a meanage and $RRPD_k = \{(m_1, l_1, c_1), \dots, (m_n, l_n, c_n)\}$ a *rotated and rescaled persistence diagram* (RRPD). The top panels of Figure 3 show an example of a PD_1 and its corresponding $RRPD_1$.

Now, we define the *accumulative persistence function* (APF) by

$$APF_k(m) = \sum_{i=1}^n c_i l_i 1(m_i \leq m), \quad m \geq 0, \quad (1)$$

where $1(\cdot)$ is the indicator function and we suppress in the notation that APF_k is a function of $RRPD_k$. Figure 1 shows the APF_0 and APF_1 associated to the brain artery tree shown in the left panel. Formally speaking, when $RRPD_k$ is considered to be random, it is viewed as a finite point process with multiplicities, see e.g. Daley and Vere-Jones (2003). It will always be clear from the context whether PD_k and $RRPD_k$ are considered as being random or observed, and hence whether APF_k is a deterministic or random function.

Clearly, $RRPD_k$ is in one-to-one correspondence to PD_k . In turn, if all $c_i = 1$ and the m_i are pairwise distinct — as noticed at the end of Section 2.1 this is often the case — then there is a one-to-one correspondence between $RRPD_k$ and its corresponding APF_k . In contrast, the dominant function, the silhouette, and the intensity estimate (see Section 1.1) are in general not in a one-to-one correspondence with $RRPD_k$. Like

these functions, APF_k is a one-dimensional function, and so it is easier to handle than the sequence of functions for the persistent landscape in Bubenik (2015) and the intensity estimate in Chen *et al.* (2015) — e.g. confidence regions become easier to plot. Contrary to the dominant function and the silhouette, the APF provides information about topological features without distinguishing between long and short lifetimes.

1.3 Outline

Our paper discusses various methods based on APFs in different contexts and illustrated in Examples 1, 2, 3, 5, 7, 9, and 10 by simulation studies related to spatial point process applications, and in Examples 4, 6, and 8 by re-analysing the brain artery trees dataset previously analysed in Bendich *et al.* (2016). Section 2 specifies the setting for these examples. Section 3 presents methods for constructing confidence regions for a single APF_k , where one method is based on existing results for a confidence region of PD_k and another concerns model assessment when fitting spatial point process models. Section 4 deals with a sample of APF_k s and considers first functional boxplots and second a bootstrap method for the construction of a confidence region for the mean of the sample. Section 5 provides different methods for comparing groups of APF_k s, using a two sample test, clustering, and supervised classification. Finally, technical proofs are deferred to Appendix A.

1.4 Software

All the computations have been made with the **R**-package TDA. In Examples 1-10, additional **R**-packages are required such as `spatstat` or `fda`. The code used in our examples is available at <http://people.math.aau.dk/~christophe/Rcode.zip>.

2 Datasets

2.1 Simulated data

In our simulation studies we consider a planar point cloud, i.e. a finite point pattern $\{x_1, \dots, x_N\} \subset \mathbb{R}^2$, and let $C_t = \{x \in \mathbb{R}^2 : \min_i \|x - x_i\| \leq t\}$, $t \geq 0$, be the sub-level sets of the distance function to the point cloud. We have this definition of C_t in mind for many "classical" applications of topological data analysis where the point cloud is sampled possibly with some noise from an unknown compact set M whose topological features are of interest (more details follow in case (i) below). Equivalently, C_t is the union of discs in \mathbb{R}^2 of radius t and centered at x_1, \dots, x_N , and we consider how the topological features of the union of discs changes as the discs grow. We expect this interpretation of C_t has more appeal to spatial statistician and stochastic geometers when it is the point pattern itself which is of interest (as explained further in case (ii))

below). By the nerve lemma, the persistence homology of $\{C_t\}_{t \geq 0}$ is given by that of the Delaunay-complex (or alpha-complex) filtration generated from $\{x_1, \dots, x_N\}$, see e.g. Edelsbrunner and Harer (2010).

We assume $\{x_1, \dots, x_N\}$ is a realisation of a point process $\mathbf{X} \subset \mathbb{R}^2$, where the count N is finite. Then PD_k and RRPD_k can be viewed as finite planar point processes (with multiplicities) and APF_k as a random function. We consider the following two settings:

- (i) N is a fixed positive integer and x_1, \dots, x_N are independent and identically distributed (IID) points on or near a compact set $M \subset \mathbb{R}^2$. Typically in applications of topological data analysis, M is unknown and the purpose is to gain information about M 's topological features by studying the persistence homology of $\{C_t\}_{t \geq 0}$. For simplicity and specificity, we let $x_i = y_i + \epsilon_i$, $i = 1, \dots, N$, where y_1, \dots, y_N are IID points on M , the noise $\epsilon_1, \dots, \epsilon_N$ are IID and independent of y_1, \dots, y_N , and ϵ_i follows the restriction to the square $[-10\sigma, 10\sigma]^2$ of a bivariate zero-mean normal distribution with IID coordinates and standard deviation $\sigma \geq 0$ (if $\sigma = 0$ there is no noise); we denote this distribution for ϵ_i by $N_2(\sigma)$ (the restriction to $[-10\sigma, 10\sigma]^2$ is only imposed for technical reasons and is not of practical importance).
- (ii) N is random and conditional on N , the points in \mathbf{X} are not necessarily IID. This is a common situation in spatial statistics, e.g. if the focus is on the point process \mathbf{X} and the purpose is to assess the goodness of fit for a specified point process model of \mathbf{X} when $\{x_1, \dots, x_N\}$ is observed.

We show that accumulated persistence functions are useful for both purposes. Setting (i) naturally applies in Example 1 of Section 3.1 and setting (ii) in Example 2 of Section 3.2. In Examples 3, 5, 7, 9, and 10 of Sections 4-5 we only consider setting (i) but setting (ii) could have been used as well when illustrating our methods.

We claim that many point process models of \mathbf{X} under setting (i) or (ii), with probability one all $c_i = 1$ and the m_i are pairwise distinct, cf. the discussion in Section 1.2 of the properties of the APF. This claim is not important for the theoretical results in the present paper, and so it will be investigated in future work.

Finally, we denote by $C((a, b), r)$ the circle with center (a, b) and radius r .

2.2 Brain artery trees dataset

The dataset in Bendich *et al.* (2016) comes from 98 brain artery trees, where one tree is excluded "as the java/matlab function crashed" (e-mail correspondence with Sean Skwerer). Each tree can be included within a cube of side length at most 206 mm and the tree is presented by a dense cloud of about 10^5 points together with edges between neighbouring points, see e.g. the left panel of Figure 1. They want to capture how the arteries bend through space and to detect age and gender effects. For $k = 0$, a Morse filtration is used: For each tree, PD_0 is obtained from the sub-level sets of the height

function; then for all meanages, $m_i \leq 137$; and the number of connected components is always below 3200. For $k = 1$, another filtration similar to that in Section 2.1 (with the plane \mathbb{R}^2 replaced by the space \mathbb{R}^3) is used: For each tree, PD_1 is obtained from the sub-level sets of the distance function to 3000 points subsampled from the tree. All the loops have a finite death time but some of them do not die during the allocated time $T = 25$; Bendich *et al.* (2016) remove these from PD_1 . Thus we shall only consider meanages $m_i \leq 25$; then the number of loops is always below 2700. For each tree and $k = 0, 1$, most $c_i = 1$ and sometimes $c_i > 1$.

For each tree and $k = 0, 1$, Bendich *et al.* (2016) use only the 100 largest lifetimes in their analysis. Whereas their principal component analysis clearly reveal age effects, their permutation test based on the mean lifetimes for the male and females subjects only shows a clear difference when considering PD_1 . Accordingly, when demonstrating the usefulness of APF_0 and APF_1 , we will focus on the gender effect and consider the same 95 trees as in Bendich *et al.* (2016) (two transsexual subjects are excluded) obtained from 46 female subjects and 49 male subjects; in contrast to Bendich *et al.* (2016), we consider all observed meanages and lifetimes. In accordance to the allocated time $T = 25$, we need to redefine APF_1 by

$$\text{APF}_1(m) = \sum_{i=1}^n c_i l_i 1(m_i \leq m, m_i + l_i/2 \leq T), \quad m \geq 0. \quad (2)$$

For simplicity we use the same notation APF_1 in (1) and (2); although all methods and results in this paper will be presented with the definition (1) in mind, they apply as well when considering (2).

Finally, we write APF_k^F and APF_k^M to distinguish between APF 's for females and males, respectively.

3 A single accumulated persistence function

3.1 Transforming confidence regions for persistence diagrams used for separating topological signal from noise

There exists several constructions and results on confidence sets for persistence diagrams when the aim is to separate topological signal from noise, see Fasy *et al.* (2014), Chazal *et al.* (2014), and the references therein. This section discusses the obvious idea of transforming such a confidence region into one for an accumulate persistence function.

We use the following notation. As in the aforementioned references, consider the persistence diagram PD_k for an unobserved manifold M (note that PD_k is considered as being non-random and unknown; of course in our simulation study presented in Example 1 below we only pretend that PD_k unknown). Let $\widehat{\text{PD}}_{k,N}$ be the random persistence diagram obtained from the sub-level sets of the distance function to IID points

x_1, \dots, x_N concentrated on or near M , where N is fixed (setting (i) in Section 2). Let $\mathcal{N} = \{(b, d) : b \leq d, l \leq 2c_N\}$ be the set of points at distance $\sqrt{2}c_N$ of the diagonal in the persistence diagram. Let $S(b, d) = \{(x, y) : |x - b| \leq c_N, |y - d| \leq c_N\}$ be the square with center (b, d) , sides parallel to the b - and d -axes, and of side length $2c_N$. Finally, let $\alpha \in (0, 1)$.

Fasy *et al.* (2014) suggest various ways of constructing a bound $c_N > 0$ so that an asymptotic conservative $(1 - \alpha)$ -confidence region for PD_k with respect to the bottleneck distance W_∞ is given by

$$\liminf_{N \rightarrow \infty} \mathbb{P} \left(W_\infty(\text{PD}_k, \widehat{\text{PD}}_{k,N}) \leq c_N \right) \geq 1 - \alpha \quad (3)$$

(here, the diagonal $\{b = d\}$ is added to PD_k). The confidence region given by (3) consists of those persistence diagrams PD_k which have exactly one point in each square $S(b_i, d_i)$, with (b_i, d_i) a point of $\widehat{\text{PD}}_{k,N}$, and have an arbitrary number of points in the set \mathcal{N} . Fasy *et al.* (2014) consider the points of $\widehat{\text{PD}}_{k,N}$ falling in \mathcal{N} as noise and the remaining points as representing a significant topological feature of M .

Using (3) an asymptotic conservative $(1 - \alpha)$ -confidence region for the APF_k corresponding to PD_k is immediately obtained. This region will be bounded by two functions $\widehat{A}_{k,N}^{\min}$ and $\widehat{A}_{k,N}^{\max}$ specified by $\widehat{\text{PD}}_{k,N}$ and c_N . Due to the accumulating nature of APF_k , the span between the bounds is an increasing function of the meanage. For a Delaunay-complex filtration or a filtration based on super-level sets of a kernel density estimate for x_1, \dots, x_N , Chazal *et al.* (2014) show that the span decreases as N increases; this is illustrated in Example 1 below.

Example 1 (simulation study). Let simply $M = C((0,0),1) \cup C((0.5,0),1)$ and suppose each point x_i is uniformly distributed on M . Figure 2 shows M and an example of a simulated point pattern with $N = 1000$ points. We use the bootstrap method implemented in the **R**-package **TDA** to compute the 95%-confidence region for PD_1 when $N = 1000$, see the top-left panel of Figure 3, where the three squares above the diagonal correspond to the three holes in M and the other squares correspond to topological noise. Thereby 95%-confidence regions for RRPD_1 (top-right panel) and APF_1 (bottom-left panel) are obtained. The confidence region for APF_1 decreases as N increases as demonstrated in the bottom panels where N is increased from 1000 to 3000.

In Figure 3 the Delaunay-complex filtration is used. If instead the filtration based on super-level sets of the kernel density estimate in Chazal *et al.* (2014) is used, then the confidence region becomes larger (for space limitations the plot is omitted).

3.2 Extreme rank envelope confidence region and test

Suppose $\mathbf{X}_0, \mathbf{X}_1, \dots, \mathbf{X}_r$ are finite spatial point processes whose joint distribution is exchangeable, i.e. for any permutation $(\sigma_0, \dots, \sigma_r)$ of $(0, \dots, r)$, $(\mathbf{X}_{\sigma_0}, \dots, \mathbf{X}_{\sigma_r})$ is distributed as $(\mathbf{X}_0, \dots, \mathbf{X}_r)$. This is a common situation for model assessment in spatial point

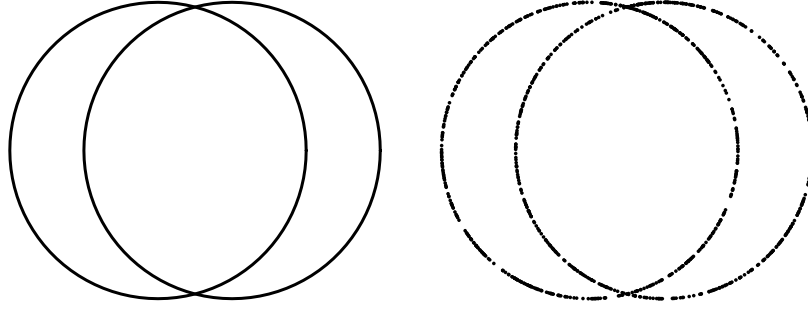


Figure 2: The set M in Example 1 (left panel) and a simulated point pattern x_1, \dots, x_{1000} of independent and uniformly distributed points on M (right panel).

process analysis where \mathbf{X}_0 has been observed and $\mathbf{X}_1, \dots, \mathbf{X}_r$ have been simulated as IID copies of \mathbf{X}_0 under a specified model for \mathbf{X}_0 , see e.g. Baddeley *et al.* (2015) and Møller and Waagepetersen (2016). For instance, in Example 2 below, $r = 2499$. Denote the APF $_k$ s for $\mathbf{X}_0, \dots, \mathbf{X}_r$ by A_0, \dots, A_r , respectively. Adapting ideas from Myllymäki *et al.* (2016), this section discusses how to construct a goodness-of-fit test and a confidence region for A_0 under the null hypothesis \mathcal{H}_0 that the joint distribution of A_0, \dots, A_r is exchangeable. The confidence region may also be useful in case the test rejects \mathcal{H}_0 .

In functional data analysis, to measure how extreme A_0 is in comparison to A_1, \dots, A_r , a so-called depth function is used for ranking A_0, \dots, A_r , see e.g. López-Pintado and Romo (2009). We suggest using a depth ordering called extreme rank in Myllymäki *et al.* (2016): Let $T > 0$ be a user-specified parameter chosen such that it is the behaviour of $A_0(m)$ for $0 \leq m \leq T$ which is of interest. For $k = 1, 2, \dots$, define the k -th bounding curves of A_0, \dots, A_r by

$$A_{\text{low}}^k(m) = \min_{i=0, \dots, r}^k A_i(m) \quad \text{and} \quad A_{\text{upp}}^k(m) = \max_{i=0, \dots, r}^k A_i(m), \quad 0 \leq m \leq T,$$

where \min^k and \max^k denote the k -th smallest and largest values, respectively, and where $k \leq r/2$. Then, for $i = 0, \dots, r$, the extreme rank of A_i with respect to A_0, \dots, A_r is

$$R_i = \max \left\{ k : A_{\text{low}}^k(m) \leq A_i(m) \leq A_{\text{upp}}^k(m) \quad \text{for all } m \in [0, T] \right\}. \quad (4)$$

The larger R_i is, the deeper or more central A_i is among A_0, \dots, A_r .

Define, for a given $\alpha \in (0, 1)$, the $(1 - \alpha)$ -extreme rank envelope as the band delimited by the curves $A_{\text{low}}^{k_\alpha}$ and $A_{\text{upp}}^{k_\alpha}$ where

$$k_\alpha = \max \left\{ k : \frac{1}{r+1} \sum_{i=0}^r 1(R_i < k) \leq \alpha \right\}.$$

Under \mathcal{H}_0 , with probability at least $1 - \alpha$,

$$A_{\text{low}}^{k_\alpha}(m) \leq A_0(m) \leq A_{\text{upp}}^{k_\alpha}(m) \quad \text{for all } m \in [0, T], \quad (5)$$

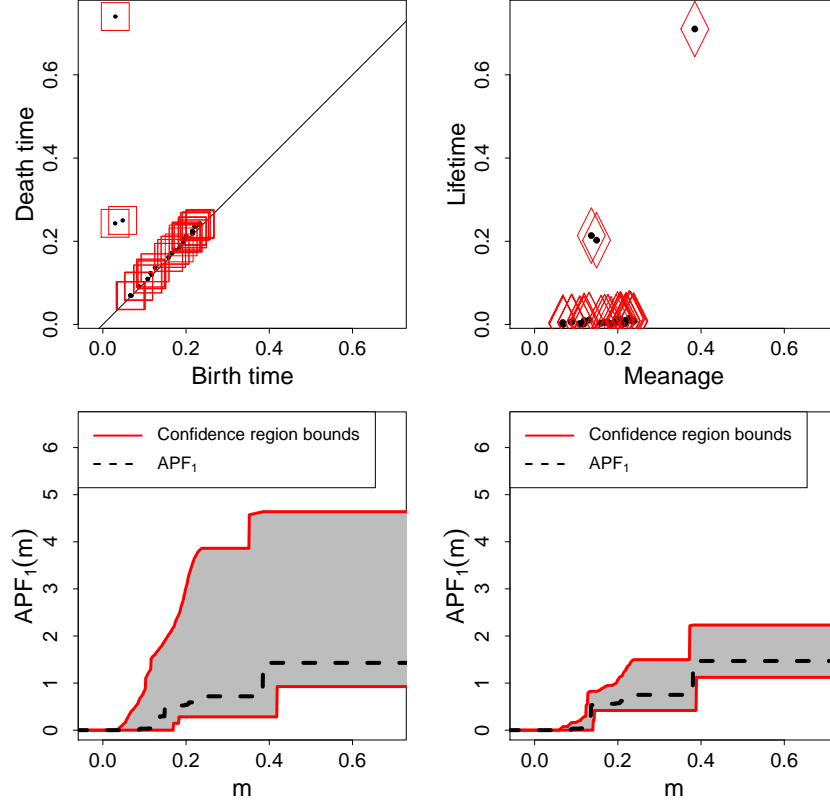


Figure 3: 95%-confidence regions obtained by the bootstrap method for PD_1 (top-left panel) and its corresponding $RRPD_1$ (top-right panel) when M and x_1, \dots, x_{1000} are as in Figure 2. The bottom-left panel shows the corresponding 95%-confidence region for APF_1 . The bottom-right panel shows the 95%-confidence region for APF_1 when a larger point cloud with 3000 points is used.

see Myllymäki *et al.* (2016). Therefore, the $(1 - \alpha)$ -extreme rank envelope is a $(1 - \alpha)$ conservative confidence region for A_0 restricted to $[0, T]$. It corresponds to a conservative statistical test called the extreme rank envelope test and which accepts \mathcal{H}_0 at level α if (5) is satisfied or equivalently if

$$\frac{1}{r+1} \sum_{i=0}^r 1(R_i < R_0) > \alpha, \quad (6)$$

cf. Myllymäki *et al.* (2016). As demonstrated in Example 2 below, in case of rejection of \mathcal{H}_0 , a plot of the extreme rank envelope allows a graphical interpretation of the extreme rank envelope test and may suggest an alternative model for the spatial point process \mathbf{X}_0 .

Indeed there exists alternatives to the extreme rank envelope test, in particular a liberal extreme rank envelope test and a so-called global scaled maximum absolute difference envelope, see Myllymäki *et al.* (2016). It is also possible to combine several extreme rank envelopes, for instance by combining APF_0 and APF_1 , see Mrkvíčka *et al.* (2016). In the following example we focus on (5)-(6) and briefly remark on results obtained by combining APF_0 and APF_1 .

Example 2 (simulation study). Recall that a homogeneous Poisson process is a model for complete spatial randomness (CSR), see e.g. Møller and Waagepetersen (2004) and the simulation in the top-left panel of Figure 4. Consider APFs A_0, A_1, \dots, A_r corresponding to independent point processes $\mathbf{X}_0, \mathbf{X}_1, \dots, \mathbf{X}_r$ defined on a unit square and where \mathbf{X}_i for $i > 0$ is CSR with a given intensity ρ (the mean number of points). Suppose \mathbf{X}_0 is claimed to be CSR with intensity ρ , however, the model for \mathbf{X}_0 is given by one of the following four point process models, which we refer to as the true model:

- (a) CSR; hence the true model agrees with the claimed model.
- (b) A Baddeley-Silverman cell process; this has the same second-order moment properties as under CSR, see Baddeley and Silverman (1984). Though from a mathematical point of view, it is a cluster process, simulated realisations will exhibit both aggregation and regularity at different scales, see the top-right panel of Figure 4.
- (c) A Matérn cluster process; this is a model for clustering where each cluster is a homogenous Poisson process within a disk and the centers of the disks are not observed and constitute a stationary Poisson process, see Matérn (1986), Møller and Waagepetersen (2004), and the bottom-left panel of Figure 4.
- (d) A most repulsive Bessel-type determinantal point process (DPP); this is a model for regularity, see Lavancier *et al.* (2015), Biscio and Lavancier (2016), and the bottom-right panel of Figure 4.

We let $\rho = 100$ or 400 . This specifies completely the models in (a) and (d), whereas the remaining parameters in the cases (b)-(c) are defined to be the same as those used in Robins and Turner (2016). In all cases of Figure 4, $\rho = 400$. Finally, following the recommendation in Myllymäki *et al.* (2016), we let $r = 2499$.

For each value of $\rho = 100$ or 400 , we simulate each point process in (a)-(d) with the **R**-package `spatstat`. Then, for each dimension $k = 0$ or 1 , we compute the extreme rank envelopes and extreme rank envelope tests with the **R**-package `spptest`. We repeat all this 500 times. Table 1 shows for each case (a)-(d) the percentage of rejection of the hypothesis that \mathbf{X}_0 is a homogeneous Poisson process with known intensity ρ . In case of CSR, the type one error of the test is small except when $k = 0$ and $\rho = 100$. As expected in case of (b)-(d), the power of the test is increased when ρ is increased. For both the Baddeley-Silverman process and the DPP, when $k = 0$ and/or $\rho = 400$, the power is high and even 100% in two cases. For the Matérn cluster process, the power is 100% when both $\rho = 100$ and 400 ; this is also the case when instead the radius of a cluster becomes 10 times larger and hence it is not so easy to distinguish the clusters as in the bottom-left panel of Figure 4. When we combine the extreme rank envelopes for APF_0 and APF_1 , the results are better or close to the best results obtained when considering only one extreme rank envelope.

Figure 5 illustrates for one of the 500 repetitions the deviation from the CSR-envelope obtained when the true model is not CSR. For $i = 0, 1$ and for each of the three non-CSR models, APF_i is outside the CSR-envelope, in particular when $i = 0$ and both the

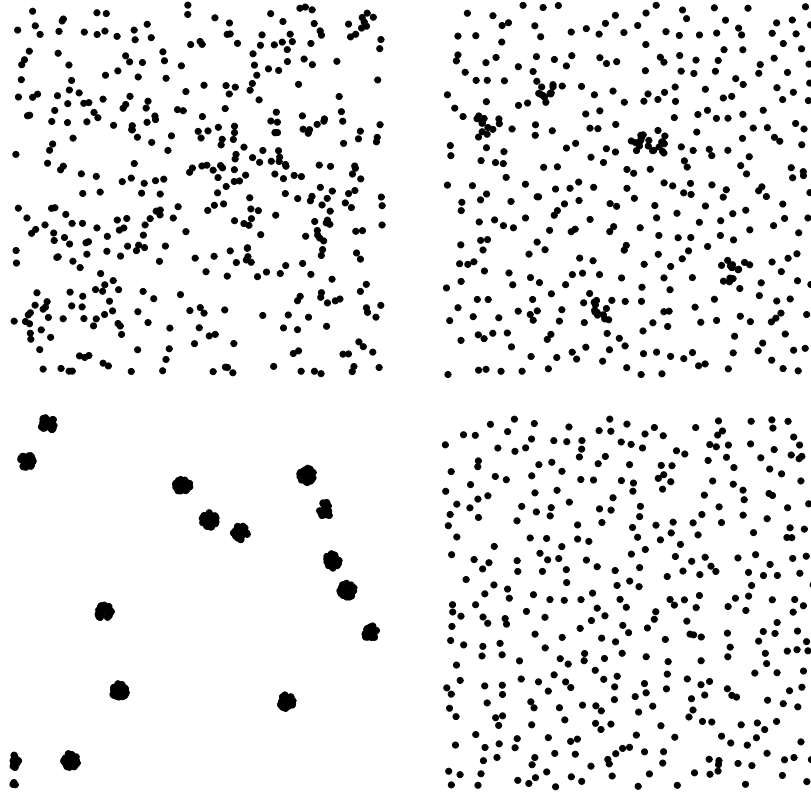


Figure 4: Simulated point patterns for a homogeneous Poisson process (top-left panel), a Baddeley-Silverman cell process (top-right panel), a Matérn cluster process (bottom-left panel), and a most repulsive Bessel-type DPP (bottom-right panel).

	CSR		DPP		Matérn cluster		Baddeley-Silverman	
	$\rho = 100$	$\rho = 400$	$\rho = 100$	$\rho = 400$	$\rho = 100$	$\rho = 400$	$\rho = 100$	$\rho = 400$
APF_0	3.6	4	77.4	100	100	100	45.6	99.6
APF_1	3.8	4.6	28.2	57.8	100	100	65.8	100
APF_0, APF_1	4.8	3.6	82.4	100	100	100	60.8	100

Table 1: Percentage of point patterns for which the 95%-extreme rank envelope test rejects the hypothesis of CSR (a homogeneous Poisson process on the unit square with intensity $\rho = 100$ or $\rho = 400$) when the true model is either CSR or one of three alternative point process models.

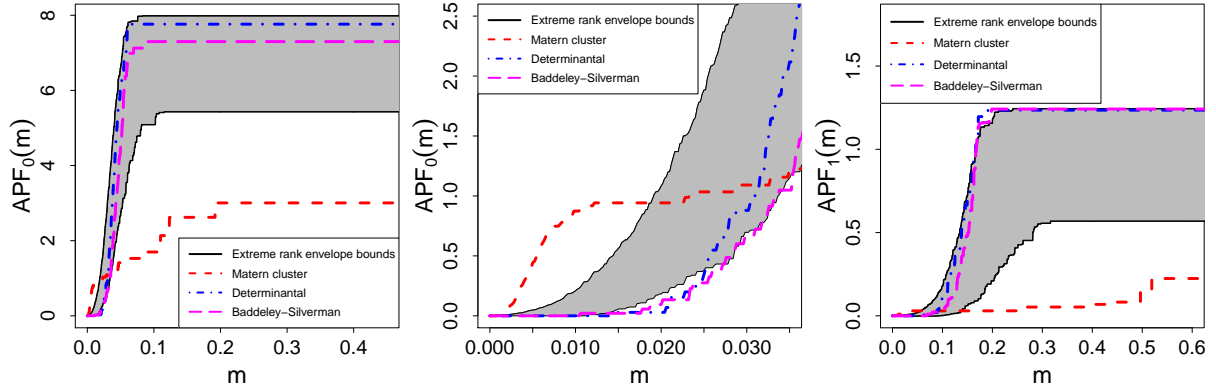


Figure 5: 95%-extreme rank envelope for APF_i when $i = 0$ (left panel and the enlargement shown in the middle panel) or $i = 1$ (right panel) together with the curves for the three non-CSR models (Baddeley-Silverman cell process, Matérn cluster process, and Bessel-type DPP). The envelope is obtained from 2499 realisations of a CSR model on the unit square and with intensity 100.

meanage and lifetime are small. This means that small lifetimes are not noise but of particular importance, cf. the discussion in Section 1.1. For the regular point process model, i.e. the DPP model in case 4), APF_0 is better to discriminate from the CSR model than APF_1 : Using an obvious notation, we may expect $APF_0^{\text{DPP}}(m) < APF_0^{\text{CSR}}(m)$ for small m and indeed this is detected by the CSR-envelope in Figure 5, whereas we may expect $APF_0^{\text{DPP}}(m) > APF_0^{\text{CSR}}(m)$ for large m though this is not detected by the CSR-envelope in Figure 5. For the aggregated point process, i.e. the Matérn cluster process in case (c), both APF_0 and APF_1 are useful: For $i = 0, 1$, we may expect $APF_i^{\text{MC}}(m) > APF_i^{\text{CSR}}(m)$ for small m , whereas $APF_i^{\text{MC}}(m) < APF_i^{\text{CSR}}(m)$ for large m , and both cases are detected by the CSR-envelope in Figure 5). For the Baddeley-Silverman cell process in case (b), we notice that APF_i^{BS} usually have a similar behavior as APF_i^{DPP} , i.e. like a regular point process, probably because clustering is a rare phenomena.

A similar simulation study is discussed in Robins and Turner (2016) for the cases (a)-(c), but notice that they fix the number of points to be 100 and they use a testing procedure based on the persistent homology rank function, which in contrast to our one-dimensional APF is a two-dimensional function and is not summarizing all the topological features represented in a persistent diagram. Robins and Turner (2016) show that a test for CSR based on the persistent homology rank function is useful as compared to various tests implemented in `spatstat` and which only concern first and second-order moment properties. Their method is in particular useful, when the true model is a Baddeley-Silverman cell process with the same first and second-order moment properties as under CSR. Comparing Figure 4 in Robins and Turner (2016) with the results in Table 1 when the true model is a Baddeley-Silverman cell process and $\rho = 100$, the extreme rank envelope test seems less powerful than the test they suggest. On the other hand, Robins and Turner (2016) observe that the latter test performs poorly when the true model is a Strauss process (a model for inhibition) or a Matérn cluster process; as noticed for the Matérn cluster process, we obtain a perfect power when using the extreme rang envelopes.

4 A single sample of accumulated persistence functions

4.1 Functional boxplot

This section discusses the use of a functional boxplot (Sun and Genton, 2011) for a sample A_1, \dots, A_r of APF_ks whose joint distribution is exchangeable. The plot provides a representation of the variation of the curves given by A_1, \dots, A_r around the most central curve, and it can be used for outlier detection, i.e. detection of curves that are too extreme with respect to the others in the sample.

The functional boxplot is based on an ordering of the APF_ks obtained using a so-called depth function. For specificity we make the standard choice called the modified band depth function (MBD), cf. López-Pintado and Romo (2009) and Sun and Genton (2011): For a user-specified parameter $T > 0$ and $h, i, j = 1, \dots, r$ with $i < j$, define

$$B_{h,i,j} = \{m \in [0, T] : \min \{A_i(m), A_j(m)\} \leq A_h(m) \leq \max \{A_i(m), A_j(m)\}\},$$

and denote the Lebesgue measure on $[0, T]$ by $|\cdot|$. Then the MBD of A_h with respect to A_1, \dots, A_r is

$$\text{MBD}_r(A_h) = \frac{2}{r(r-1)} \sum_{1 \leq i < j \leq r} |B_{h,i,j}|. \quad (7)$$

This is the average proportion of A_h on $[0, T]$ between all possible pairs of A_1, \dots, A_r . Thus, the larger the value of the MBD of a curve is, the more central or deeper it is in the sample. We call the region delimited by the 50% most central curves the central envelope. It is often assumed that a curve outside the central envelope inflated by 1.5 times the range of the central envelope is an outlier or abnormal curve — this is just a generalisation of a similar criterion for the boxplot of a sample of real numbers — and the range may be changed if it is more suitable for the application at hand, see the discussion in Sun and Genton (2011) and Example 3 below.

Below in Examples 3-4 we use the **R**-package `fda` for producing the functional boxplots: The most central curve is plotted in black, the central envelope in purple, and the upper and lower bounds obtained from all the curves except the outliers in dark blue.

Example 3 (simulation study). To illustrate how well a functional boxplot detects outliers, we consider 65 independent APF_ks, where the joint distribution of the first 50 APF_ks is exchangeable, whereas the last 15 play the role of outliers. We suppose each APF_k corresponds to a point process of 100 IID points, where each point x_i follows one of the following distributions P_1, \dots, P_4 .

- P_1 (unit circle): x_i is a uniform point on $C((0,0), 1)$ perturbed by $N_2(0.1)$ -noise.
- P_2 (Gaussian mixture): Let y_i follow $N_2(0.2)$, then $x_i = y_i$ with probability 0.5, and $x_i = y_i + (1.5, 0.5)$ otherwise.

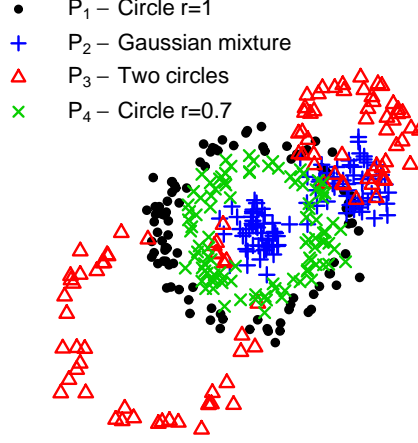


Figure 6: Simulated realizations of the four types of point processes, each consisting of 100 IID points with distribution either P_1 (black dots), P_2 (blue crosses), P_3 (red triangles), or P_4 (rotated green crosses).

- P_3 (two circles): x_i is a uniform point on $C((-1, -1), 1) \cup C((1, 1), 0.5)$ perturbed by $N_2((0, 0), 0.1)$ -noise.
- P_4 (circle of radius 0.7): x_i is a uniform point on $C((0, 0), 0.7)$ perturbed by $N_2(0.1)$ -noise.

We let the first 50 point processes be obtained from P_1 (the distribution for non-outliers), the next 5 from P_2 , the following 5 from P_3 , and the final 5 from P_4 . Figure 6 shows a simulated realization of each of the four types of point processes.

Figure 7 shows the functional boxplots when considering APF_0 (left panel) and APF_1 (right panel). The curves detected as outliers and corresponding to the distributions P_2, P_3 , and P_4 are plotted in red, blue, and green, respectively. In both panels the outliers detected by the 1.5 criterion agree with the true outliers. If we repeat everything but with the distribution P_4 redefined so that $C((0, 0), 0.7)$ is replaced by $C((0, 0), 0.8)$, then the support of P_4 is closer to that of P_1 and it becomes harder in the case of APF_0 to detect the outliers with distribution P_4 (we omit the corresponding plot); thus further simulations for determining a stronger criterion would be needed.

Example 4 (brain artery trees). For the brain artery trees dataset (Section 2.2), Figure 8 shows the functional boxplots of APFs for females (left panels) respective males (right panels) when $k = 0$ (top panels) and $k = 1$ (bottom panels). Comparing the top panels (concerned with connected components), the shape of the central envelope is clearly different for females and males, in particular on the interval $[40, 60]$, and the upper and lower bounds of the non-outlier are closer to the central region for females, in particular on the interval $[0, 50]$. For the bottom panels (concerned with loops), the main difference is observed on the interval $[15, 25]$ where the central envelope is larger for females than for males.

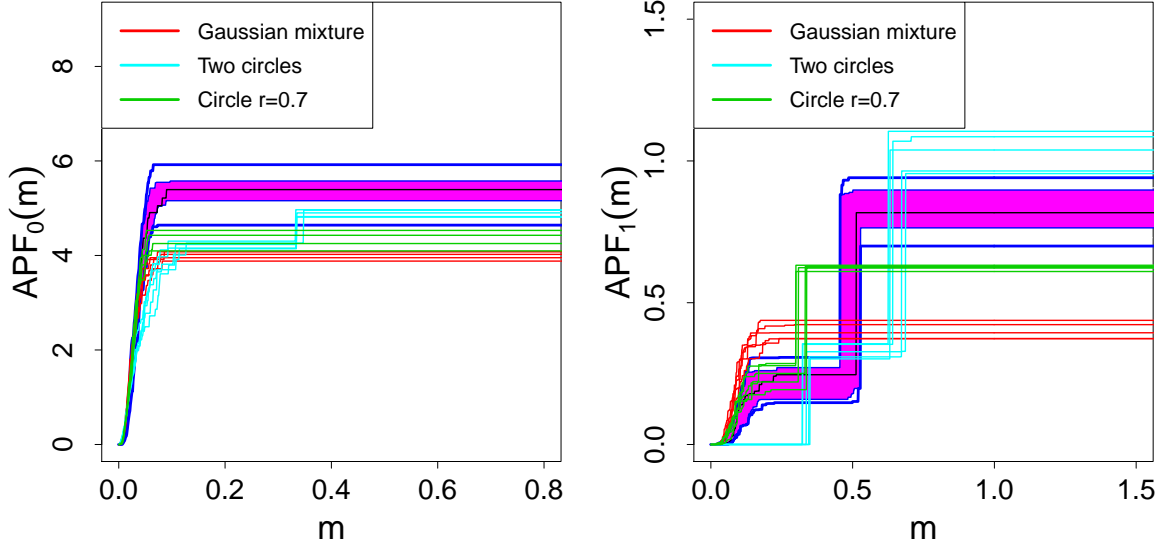


Figure 7: Functional boxplots of 65 APFs based on the topological features of dimension 0 (left panel) and 1 (right panel). In each panel, 50, 5, 5, and 5 APFs are obtained from the sub-level sets of the distance function to 100 IID points from the distribution P_1 , P_2 , P_3 , and P_4 , respectively. The APFs detected as outliers are plotted in red, blue, and green in the case of P_2 , P_3 , and P_4 , respectively.

The dashed lines in Figure 8 show the APFs detected as outliers by the 1.5 criterion, that is 6 APF_0^F s (top-left panel), 3 APF_1^F s (bottom-left panel), 6 APF_0^M s (top-right panel), and 4 APF_1^M s (bottom-right panel). For the females, only for one point pattern both APF_0^F and APF_1^F are outliers, where APF_1^F is the steep dashed line in the bottom-left panel; and for the males, only for two point patterns both APF_0^M and APF_1^M are outliers, where in one case APF_1^M is the steep dashed line in the bottom-right panel. For this case, Figure 9 reveals an obvious issue: A large part on the right of the corresponding tree is missing!

In Examples 6 and 8 we discuss to what extent our analysis of the brain artery trees will be sensitive to whether we include or exclude the detected outliers.

4.2 Confidence region for the mean function

This section considers an asymptotic confidence region for the mean function of a sample A_1, \dots, A_r of IID APF_k s. We assume that D_1, \dots, D_r are the underlying IID $RRPD_k$ s for the sample so that with probability one, there exists an upper bound $T < \infty$ on the death times and there exists an upper bound $n_{\max} < \infty$ on the number of k -dimensional topological features. Note that the state space for such $RRPD_k$ s is

$$\mathcal{D}_{k,T,n_{\max}} = \left\{ \{(m_1, l_1, c_1), \dots, (m_n, l_n, c_n)\} : \sum_{i=1}^n c_i \leq n_{\max}, m_i + l_i/2 \leq T, i = 1, \dots, n \right\}$$

and only the existence and not the actual values of n_{\max} and T play a role when applying our method below. For example, in the settings (i)-(ii) of Section 2.1 it suffices

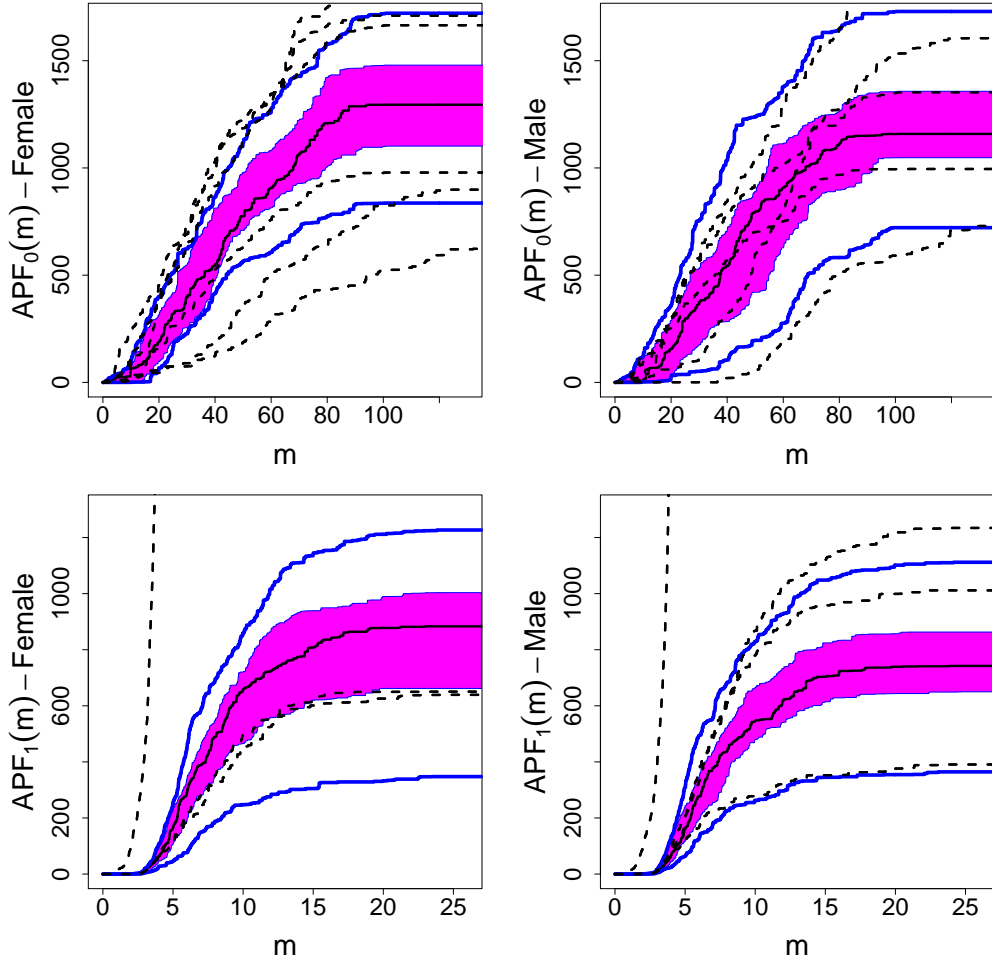


Figure 8: Functional boxplots of APFs for females and males obtained from the brain artery trees dataset: APF_0^F (top-left panel), APF_0^M (top-right panel), APF_1^F (bottom-left panel), APF_1^M (bottom-right panel). The dashed lines show the outliers detected by the 1.5 criterion.



Figure 9: Brain artery tree of a male subject with APF_0^M and APF_1^M detected as outliers by the 1.5 criterion.

to assume that \mathbf{X} is included in a bounded region of \mathbb{R}^2 and that the number of points N is bounded by a constant; this follows from the two versions of the nerve lemma presented in Fasy *et al.* (2014) and Edelsbrunner and Harer (2010), respectively.

We adapt an empirical bootstrap procedure (see e.g. van der Vaart and Wellner (1996)) which in Chazal *et al.* (2013) is used for a confidence region for the mean of the dominant function of the persistent landscape and which in our case works as follows. For $0 \leq m \leq T$, the mean function is given by $\mu(m) = \mathbb{E}\{A_1(m)\}$ and estimated by the empirical mean function $\bar{A}_r(m) = \frac{1}{r} \sum_{i=1}^r A_i(m)$. Let A_1^*, \dots, A_r^* be independent uniform draws from the set $\{A_1, \dots, A_r\}$ and set $\bar{A}_r^* = \frac{1}{r} \sum_{i=1}^r A_i^*$ and $\theta^* = \sup_{m \in [0, T]} \sqrt{r} |\bar{A}_r(m) - \bar{A}_r^*(m)|$. For a given integer $B > 0$, independently repeat this procedure B times to obtain $\theta_1^*, \dots, \theta_B^*$. Then, for $0 < \alpha < 1$, the $(1 - \alpha)$ -quantile in the distribution of θ^* is estimated by

$$\hat{q}_\alpha^B = \inf\{q \geq 0 : \frac{1}{B} \sum_{i=1}^B 1(\theta_i^* > q) \leq \alpha\}.$$

The following theorem is verified in Appendix A.

Theorem 4.1. *Let the situation be as described above. For large values of r and B , the functions $\bar{A}_r \pm \hat{q}_\alpha^B / \sqrt{r}$ provide the bounds for an asymptotic conservative $(1 - \alpha)$ -confidence region for the mean APF, that is*

$$\lim_{r \rightarrow \infty} \lim_{B \rightarrow \infty} \mathbb{P} \left(\sup_{m \in [0, T]} |\mu(m) - \bar{A}_r(m)| \leq \hat{q}_\alpha^B / \sqrt{r} \right) \geq 1 - \alpha.$$

Example 5 (simulation study). Consider $r = 50$ IID copies of a point process consisting of 100 independent and uniformly distributed points on the union of three circles with radius 0.25 and centred at $(-1, -1)$, $(0, 1)$, and $(1, -1)$, respectively. A simulated realization of the point process is shown in the left panel of Figure 10, and the next two panels show simulated confidence regions for APF_0 and APF_1 , respectively, when the bootstrap procedure with $B = 1000$ is used. In the middle panel, between $m = 0$ and $m = 0.2$, there is an accumulation of small jumps corresponding to the moment when each circle is covered by the union of growing discs from the Delaunay-complex filtration; we interpret these small jumps as topological noise. The jump at $m \simeq 0.25$ corresponds to the moment when the circles centred at $(-1, 1)$ and $(1, -1)$ are connected by the growing discs, and the jump at $m \simeq 0.3$ to when all three circles are connected by the growing discs. In the right panel, at $m \simeq 0.3$ there is an accumulation of small jumps corresponding to the moment when the three circles are connected by the growing discs and they form a hole at the centre. The disappearance of this hole corresponds to the jump at $m \simeq 0.7$.

Example 6 (brain artery trees). The brain artery trees are all contained in a bounded region and presented by a bounded number of points, so it is obvious that T and n_{\max} exist for $k = 0, 1$. To establish confidence regions for the mean of the APF_k^M s respective

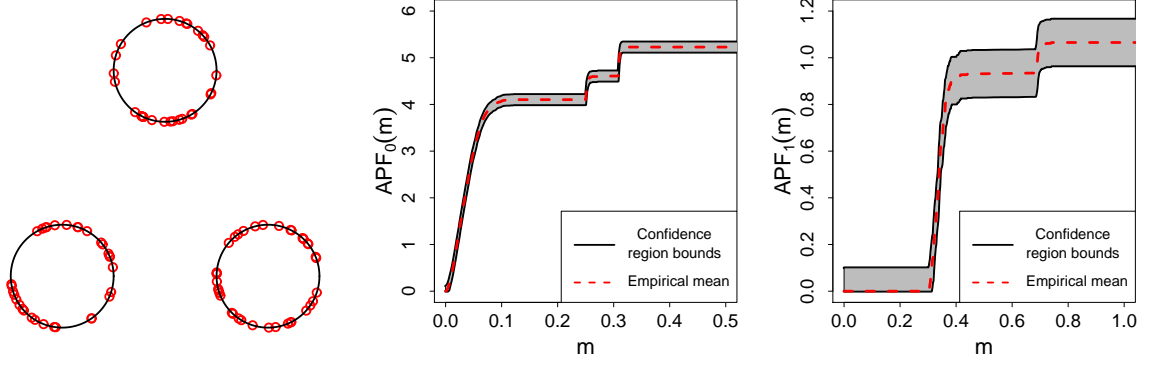


Figure 10: A simulation of 100 independent and uniformly distributed points on the union of three circles (dashed lines) with the same radius $r = 0.5$ and centred at $(-1, -1)$, $(0, 1)$, and $(1, -1)$ (left panel). The 95%-confidence regions for the mean APF_0 (middle panel) and the mean APF_1 (right panel) are based on 50 IID simulations.

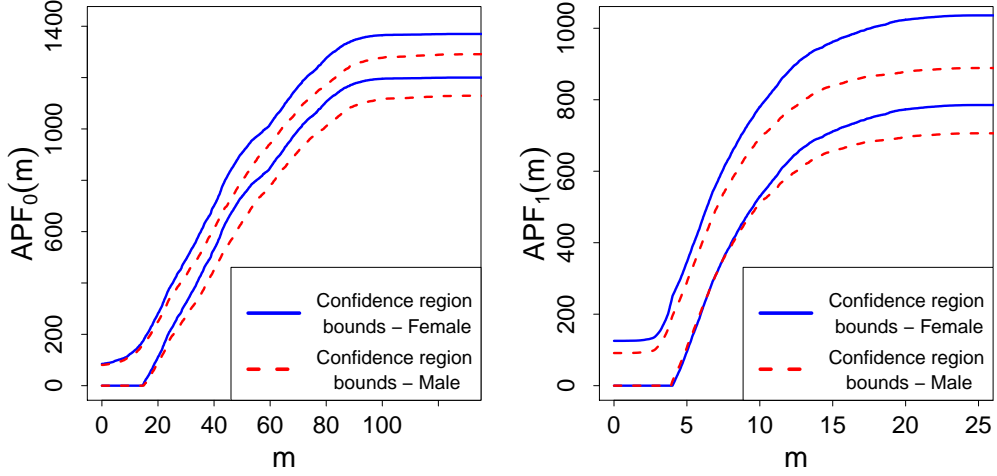


Figure 11: Bootstrap confidence regions for the mean APF_k^M and APF_k^F when $k = 0$ (left panel) and $k = 1$ (right panel).

APF_k^F s, we apply the bootstrap procedure with $B = 1000$. The result is shown in Figure 11 when all 95 trees are considered: In the left panel, $k = 0$ and approximately half of each confidence region overlap with the other confidence region; it is not clear if there is a difference between genders. In the right panel, $k = 1$ and the difference is more pronounced, in particular on the interval $[15, 25]$. Similar results and conclusions are obtained if we exclude the APFs detected as outliers in Example 4. Of course we should supply with a statistical test to assess the gender effect and such a test is established in Section 5.1 and applied in Example 8.

5 Two or more samples of accumulated persistence functions

5.1 A two-sample test

Consider two samples of independent RRPD_ks D_1, \dots, D_{r_1} and E_1, \dots, E_{r_2} , where each D_i ($i = 1, \dots, r_1$) has distribution P_D and each E_j has distribution P_E ($j = 1, \dots, r_2$), and suppose we want to test the null hypothesis $\mathcal{H}_0: P_D = P_E = P$. Here, the common distribution P is unknown and as in Section 4.2 we assume it is concentrated on $\mathcal{D}_{k,T,n_{\max}}$ for some integer $n_{\max} > 0$ and number $T > 0$. Below, we adapt a two-sample test statistic studied in Præstgaard (1995) and van der Vaart and Wellner (1996).

Let $r = r_1 + r_2$. Let A_1, \dots, A_r be the APF_k corresponding to $(D_1, \dots, D_{r_1}, E_1, \dots, E_{r_2})$, and denote by \overline{A}_{r_1} and \overline{A}_{r_2} the empirical means of A_1, \dots, A_{r_1} and $A_{r_1+1}, \dots, A_{r_1+r_2}$, respectively. Let $I = [T_1, T_2]$ be a user-specified interval with $0 \leq T_1 < T_2 \leq T$ and used for defining a two-sample test statistic by

$$KS_{r_1, r_2} = \sqrt{\frac{r_1 r_2}{r}} \sup_{m \in I} |\overline{A}_{r_1}(m) - \overline{A}_{r_2}(m)|, \quad (8)$$

where large values are critical for \mathcal{H}_0 . This may be rewritten as

$$KS_{r_1, r_2} = \sup_{m \in I} \left| \sqrt{\frac{r_2}{r}} G_D^{r_1}(m) - \sqrt{\frac{r_1}{r}} G_E^{r_2}(m) + \sqrt{\frac{r_1 r_2}{r}} E\{A_D - A_E\}(m) \right|, \quad (9)$$

where $G_D^{r_1} = \sqrt{r_1} (\overline{A}_{r_1} - E\{A_D\})$ and $G_E^{r_2} = \sqrt{r_2} (\overline{A}_{r_2} - E\{A_E\})$. By Lemma A.2 in Appendix A and by the independence of the samples, $G_D^{r_1}$ and $G_E^{r_2}$ converge in distribution to two independent zero-mean Gaussian processes on I , denoted G_D and G_E , respectively. Assume that $r_1/r \rightarrow \lambda \in (0, 1)$ as $r \rightarrow \infty$. Under \mathcal{H}_0 , in the sense of convergence in distribution,

$$\lim_{r \rightarrow \infty} KS_{r_1, r_2} = \sup_{m \in I} |\sqrt{1-\lambda} G_D(m) - \sqrt{\lambda} G_E(m)|, \quad (10)$$

where $\sqrt{1-\lambda} G_D - \sqrt{\lambda} G_E$ follows the same distribution as G_D . If \mathcal{H}_0 is not true and $\sup_{m \in I} |E\{A_1 - A_{r_1+1}\}(m)| > 0$, then $KS_{r_1, r_2} \rightarrow \infty$ as $r \rightarrow \infty$, see van der Vaart and Wellner (1996). Therefore, for $0 < \alpha < 1$ and letting $q_\alpha = \inf\{q : P(\sup_{m \in I} |G_D(m)| > q) \leq \alpha\}$, the asymptotic test that rejects \mathcal{H}_0 if $KS_{r_1, r_2} \leq q_\alpha$ is of level α and of power 1.

As q_α depends on the unknown distribution P , we estimate q_α by a bootstrap method as follows. Let A_1^*, \dots, A_r^* be independent uniform draws from $\{A_1, \dots, A_r\}$. For $0 \leq m \leq T$, define the empirical mean functions $\overline{A}_{r_1}^*(m) = \frac{1}{r_1} \sum_{i=1}^{r_1} A_i^*(m)$ and $\overline{A}_{r_2}^*(m) = \frac{1}{r_2} \sum_{i=r_1+1}^{r_1+r_2} A_i^*(m)$, and compute

$$\theta^* = \sqrt{\frac{r_1 r_2}{r}} \sup_{m \in I} |\overline{A}_{r_1}^*(m) - \overline{A}_{r_2}^*(m)|. \quad (11)$$

For a given integer $B > 0$, independently repeat this procedure B times to obtain $\theta_1^*, \dots, \theta_B^*$. Then we estimate q_α by the $(1 - \alpha)$ -quantile of the empirical distribution of $\theta_1^*, \dots, \theta_B^*$, that is

$$\hat{q}_\alpha^B = \inf\{q \geq 0 : \frac{1}{B} \sum_{i=1}^B 1(\theta_i^* > q) \leq \alpha\}.$$

The next theorem is a direct application of Theorem 3.7.7 in van der Vaart and Wellner (1996) noticing that the APF_k s are uniformly bounded by Tn_{\max} and they form a so-called Donsker class, see Lemma A.2 and its proof in Appendix A.

Theorem 5.1. *Let the situation be as described above. If $r \rightarrow \infty$ such that $r_1/r \rightarrow \lambda$ with $\lambda \in (0, 1)$, then under \mathcal{H}_0*

$$\lim_{r \rightarrow \infty} \lim_{B \rightarrow \infty} \mathbb{P} \left(KS_{r_1, r_2} > \hat{q}_\alpha^B \right) = \alpha,$$

whilst if \mathcal{H}_0 is not true and $\sup_{m \in I} |\mathbb{E} \{A_1 - A_{r_1+1}\}(m)| > 0$, then

$$\lim_{r \rightarrow \infty} \lim_{B \rightarrow \infty} \mathbb{P} \left(KS_{r_1, r_2} > \hat{q}_\alpha^B \right) = 1.$$

Therefore, the test that rejects \mathcal{H}_0 if $KS_{r_1, r_2} > \hat{q}_\alpha^B$ is of asymptotic level α and power 1. Other two-sample test statistics than (8) can be constructed by considering other measurable functions of $\overline{A_{r_1}} - \overline{A_{r_2}}$, e.g. we may consider the two-sample test statistic

$$M_{r_1, r_2} = \int_I |\overline{A_{r_1}}(m) - \overline{A_{r_2}}(m)| \, dm. \quad (12)$$

Then by similar arguments as above but redefining θ^* in (11) by

$$\theta^* = \sqrt{\frac{r_1 r_2}{r}} \int_{m \in I} |\overline{A_{r_1}^*}(m) - \overline{A_{r_2}^*}(m)| \, dm,$$

the test that rejects \mathcal{H}_0 if $M_{r_1, r_2} > \hat{q}_\alpha^B$ is of asymptotic level α and power 1.

Example 7 (simulation study). Let P_D be the distribution of a RRPD_k obtained from 100 independent and uniformly distributed points on $C((0, 0), 1)$ perturbed by $N_2(0.2)$ -noise, and define P_E in a similar way but with a circle of radius 0.95. A simulated realisation of each point process is shown in Figure 12; it seems difficult to recognize that the underlying circles are different. Let us consider the two-sample test statistics (8) and (12) with $I = [0, 3]$, $r_1 = r_2 = 50$, and $\alpha = 5\%$. Over 500 simulations of the two samples of RRPD_k we obtain the following percentage of rejection: For M_{r_1, r_2} , 5.2% if $k = 0$, and 24.2% if $k = 1$. For KS_{r_1, r_2} much better results are observed, namely 73.8% if $k = 0$, and 93.8% if $k = 1$, where this high percentage is mainly caused by the largest lifetime of a loop.

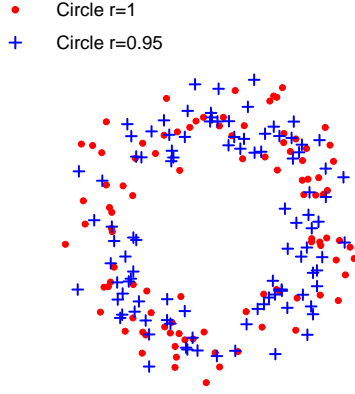


Figure 12: A simulation of 100 independent and uniformly distributed points on the circle centred at $(0,0)$ with radius 1 and perturbed by $N_2((0,0), 0.2)$ -noise (red dots), together with 100 independent and uniformly distributed points on the circle centred at $(0,0)$ with radius 0.95 and perturbed by $N_2((0,0), 0.2)$ -noise (blue crosses).

Example 8 (brain artery trees). To distinguish between male and female subjects of the brain artery trees dataset, we use the two-sample test statistic KS_{r_1, r_2} under three different settings:

- (A) For $k = 0, 1$, we let PD'_k be the subset of PD_k corresponding to the 100 largest lifetimes. Then D_1, \dots, D_{46} and E_1, \dots, E_{49} are the $RRPD_k$ s obtained from the PD'_k s associated to female and male subjects, respectively. This is the setting used in Bendich *et al.* (2016).
- (B) For $k = 0, 1$, we consider all lifetimes and let D_1, \dots, D_{46} and E_1, \dots, E_{49} be the $RRPD_k$ s associated to female and male subjects, respectively.
- (C) The samples are as in setting (B) except that we exclude the $RRPD_k$ s where the corresponding APF_k was detected as an outlier in Example 4. Hence, $r_1 = 40$ and $r_2 = 43$ if $k = 0$, and $r_1 = 43$ and $r_2 = 45$ if $k = 1$.

Bendich *et al.* (2016) perform a permutation test based on the mean lifetimes for the male and female subjects and conclude that gender effect is recognized when considering PD_1 (p -value = 3%) but not PD_0 (p -value = 10%). For comparison, under each setting (A)-(C), we perform the two-sample test for $k = 0, 1$, different intervals I , and $B = 10000$. In each case, we estimate the p -value, i.e. the smallest α such that the two-sample test with significance level α does not reject \mathcal{H}_0 , by $\hat{p} = \frac{1}{B} \sum_{i=1}^B 1(\theta_i^* > KS_{r_1, r_2})$. Table 2 shows the results. Under each setting (A)-(C), using APF_0 we have a smaller p -value than in Bendich *et al.* (2016) if $I = [0, 137]$ and an even larger p -value if $I = [0, 60]$; and for $k = 1$ under setting (B), our p -value is about seven times larger than the p -value in Bendich *et al.* (2016) if $I = [0, 25]$, and else it is similar or smaller. For $k = 1$ and $I = [0, 25]$, the large difference between our p -values under settings (B) and (C) indicates that the presence of outliers violates the result of Theorem 5.1 and care should hence be taken. In our opinion we can better trust the results without outliers, where in contrast to Bendich *et al.* (2016) we see a clear gender effect when considering the connected components. Notice also that in agreement with the discussion of Figure 8 in Example 4, for each setting A, B, and C and each dimension $k = 0, 1$, the p -values in

	APF ₀		APF ₁	
	$I = [0, 137]$	$I = [0, 60]$	$I = [0, 25]$	$I = [15, 25]$
Setting (A)	5.26	3.26	3.18	2.72
Setting (B)	7.67	3.64	20.06	1.83
Setting (C)	4.55	2.61	0.92	0.85

Table 2: Estimated p -values of the two-sample test based on KS_{r_1, r_2} used with APF₀ and APF₁ on different intervals I to distinguish between male and female subjects under settings (A), (B), and (C) described in Example 8.

Table 2 are smallest when considering the smaller interval $I = [0, 60]$ or $I = [15, 25]$.

5.2 Clustering

Suppose A_1, \dots, A_r are APF _{k} s which we want to label into $K < r$ groups by using a method of clustering (or unsupervised classification). Such methods are studied many places in the literature for functional data, see the survey in Jacques and Preda (2014); Chazal *et al.* (2009), Chen *et al.* (2015), and Robins and Turner (2016) consider clustering in connection to RRPD _{k} s. Whereas the RRPD _{k} s are two-dimensional functions, it becomes easy to use clustering for the one-dimensional APF _{k} s as illustrated in Example 9 below.

For simplicity we just consider the standard technique known as the K -means clustering algorithm (Hartigan and Wong (1979)): Assume that A_1, \dots, A_r are pairwise different and square-integrable functions on $[0, T]$, where T is a user-specified parameter. For example, if $RRPD_k \in \mathcal{D}_{k, T, n_{\max}}$ (see Section 4.2), then $APF_k \in L^2([0, T])$. The K -means clustering algorithm works as follows.

- Chose uniformly at random a subset of K functions from $\{A_1, \dots, A_r\}$; call these functions centres and label them by $1, \dots, K$.
- Assign each non-selected APF _{k} the label i if it is closer to the centre of label i than to any other centre with respect to the L^2 -distance on $L^2([0, T])$.
- In each group, reassign the centre by the mean curve of the group (this may not be an APF _{k} of the sample).
- Iterate these steps until the assignment of centres does not change.

The algorithm is known to be convergent, however, it may have several drawbacks as discussed in Hartigan and Wong (1979) and Bottou and Bengio (1995).

Example 9 (simulation study). Consider $K = 3$ groups, each consisting of 50 APF₀s and associated to point processes consisting of 100 IID points, where each point x_i follows one of the following distributions P_1 , P_2 , and P_3 for groups 1, 2, and 3, respectively.

- P_1 (unit circle): x_i is a uniform point on $C((0,0),1)$ perturbed by $N_2(0.1)$ -noise.
- P_2 (two circles): x_i is a uniform point on $C((-1,-1),0.5) \cup C((1,1),0.5)$ perturbed by $N_2(0.1)$ -noise.
- P_3 (circle of radius 0.8): x_i is a uniform point on $C((0,0),0.8)$ perturbed by $N_2(0.1)$ -noise.

We start by simulating a realization of each of the $3 \times 50 = 150$ point processes. The left panel of Figure 13 shows one realization of each type of point process; it seems difficult to distinguish the underlying circles for groups 1 and 3, but the three APF₀s associated to these three point patterns are in fact assigned to their right groups. The right panel of Figure 13 shows the result of the K -means clustering algorithm. Here we are using the **R**-function “kmeans” for the K -means algorithm and it takes only a few seconds when evaluating each $A_i(m)$ at 2500 equidistant values of m between 0 and $T = 0.5$. As expected we see more overlap between the curves of the APF₀s assigned to groups 1 and 3.

We next repeat 500 times the simulation of the 150 point processes. A clear distinction between the groups is obtained by the K -means algorithm applied for connected components: The percentage of wrongly assigned APF₀s among the $500 \times 3 \times 50 = 75000$ APF₀s has an average of 4.5% and a standard deviation of 1.6%. The assignment error is in fact mostly caused by incorrect labelling of APF₀s associated to P_1 or P_3 .

Even better results are obtained when considering loops instead of connected components: The percentage of wrongly assigned APF₁s among the 75000 APF₁s has an average of 1.6% and a standard deviation of 1.0%.

5.3 Supervised classification

Suppose we want to assign an APF _{k} to a training set of K different groups $\mathcal{G}_1, \dots, \mathcal{G}_K$, where \mathcal{G}_i is a sample of r_i independent APF _{k} s $A_1^i, \dots, A_{r_i}^i$. For this purpose supervised classification methods for functional data may be adapted.

We just consider a particular method by López-Pintado *et al.* (2010): Suppose we believe that at least $(1 - \alpha)\%$ of the APF _{k} s in each group are IID, whereas the remaining APF _{k} s in each group follow a different distribution and are considered as outliers (see Section 4.1). For a user-specified parameter $T > 0$ and $i = 1, \dots, K$, define the α -trimmed mean \bar{A}_i^α with respect to \mathcal{G}_i as the mean function on $[0, T]$ of the $(1 - \alpha)\%$ APF _{k} s in \mathcal{G}_i with the largest MBD _{r_i} , see (7). Assuming $\cup_{i=1}^K \mathcal{G}_i \subset L^2([0, T])$, an APF _{k}

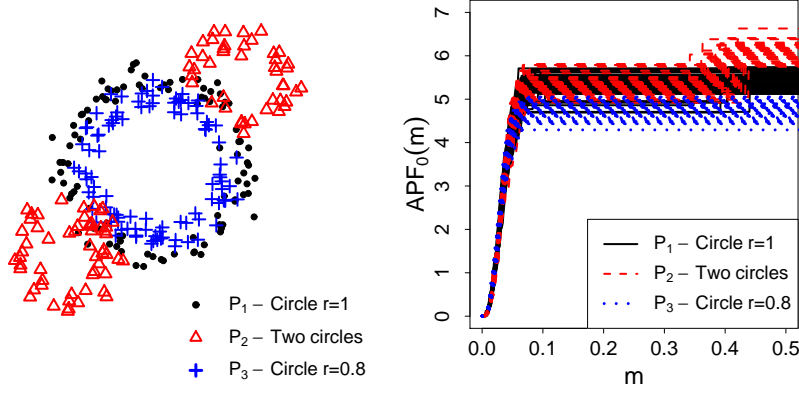


Figure 13: Left panel: Simulated example of the three point processes, each consisting of 100 IID points drawn from the distribution P_1 (black dots), P_2 (red triangles), or P_3 (blue crosses). Right panel: The 150 APF_0 s obtained from the simulation of the 150 point processes associated to P_1 , P_2 , or P_3 , where the colouring in black, red, or blue specifies whether the K -means algorithm assigns an APF_0 to the group associated to P_1 , P_2 , or P_3 .

$A \in L^2([0, T])$ is assigned to \mathcal{G}_i if

$$i = \underset{j \in \{1, \dots, K\}}{\operatorname{argmin}} \|\bar{A}_j^\alpha - A\|, \quad (13)$$

where $\|\cdot\|$ denotes the L^2 -distance.

Example 10 (simulation study). Consider the following distributions P_1, \dots, P_4 for a point x_i .

- P_1 (unit circle): x_i is a uniform point on $C((0, 0), 1)$ which is perturbed by N_2 (0.1)-noise.
- P'_1 (two circles, radii 1 and 0.5): x_i is a uniform point on $C((0, 0), 1) \cup C((1.5, 1.5), 0.5)$ and perturbed by N_2 (0.1)-noise.
- P_2 (circle of radius 0.8): x_i is a uniform point on $C((0, 0), 0.8)$ which is perturbed by N_2 (0.1)-noise.
- P'_2 (two circles, radii 0.8 and 0.5): x_i is a uniform point on $C((0, 0), 0.8) \cup C((1.5, 1.5), 0.5)$ and perturbed by N_2 (0.1)-noise.

For $k = 0, 1$ we consider the following simulation study: $K = 2$ and $r_1 = r_2 = 50$; \mathcal{G}_1 consists of 45 APF_k s associated to simulations of point processes consisting of 100 IID points with distribution P_1 (the non-outliers) and 5 APF_k s obtained in the same way but from P'_1 (the outliers); \mathcal{G}_2 is specified in the same way as \mathcal{G}_1 but replacing P_1 and P'_1 with P_2 and P'_2 , respectively; and we have correctly specified that $\alpha = 0.2$. Then we simulate 100 APF_k s associated to P_1 and 100 APF_k s associated to P_2 , i.e. they are all non-outliers. Finally, we use (13) to assign each of these 200 APF_k s to either \mathcal{G}_1 or \mathcal{G}_2 .

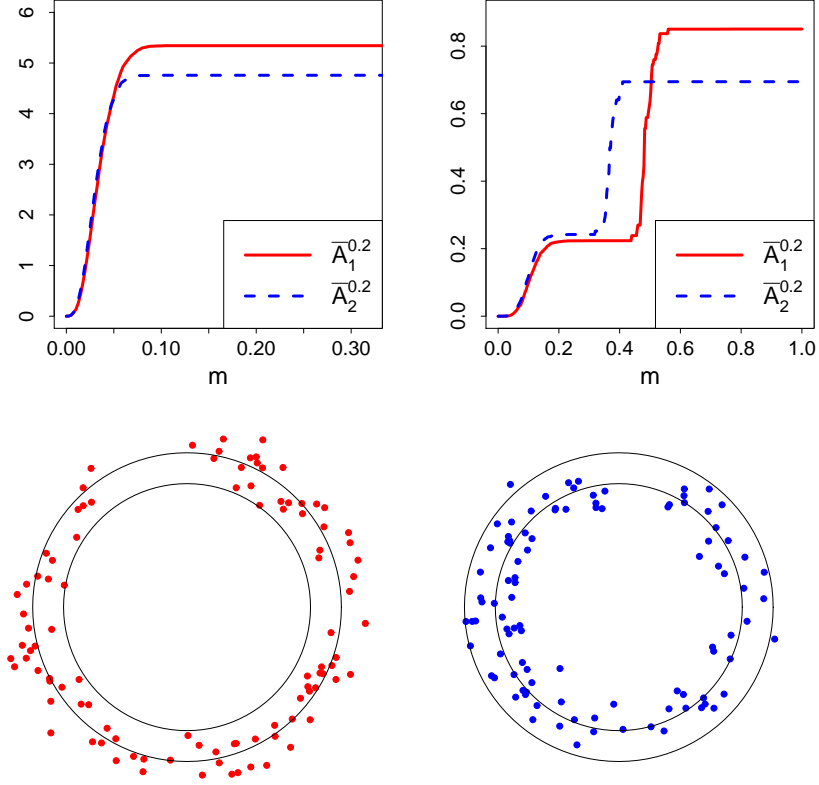


Figure 14: Top panels: The 20%-trimmed mean functions with respect to \mathcal{G}_1 and \mathcal{G}_2 when considering APF₀s (left) and APF₁s (right) obtained from the sub-level sets of the distance function to 100 IID points following the distribution P_1 (solid curve) or P_2 (dotted curve). Bottom panels: Examples of point patterns with associated APF₀s assigned to the wrong group, together with the circles of radius 0.8 and 1.

The top panels in Figure 14 show the α -trimmed means $\bar{A}_1^{0.2}$ and $\bar{A}_2^{0.2}$ when $k = 0$ (left) and $k = 1$ (right). The difference between the α -trimmed means is clearest when $k = 1$ and so we expect that the assignment error is lower in that case. In fact wrong assignments happen mainly when the support of P_1 or P_2 is not well covered by the point pattern as illustrated in the bottom panels.

Repeating this simulation study 500 times, the percentage of APF₀s wrongly assigned among the 500 repetitions has a mean of 6.7% and a standard deviation of 1.7%, whereas for the APF₁s the mean is 0.24% and the standard deviation is 0.43%. To investigate how the results depend on the radius of the smallest circle, we repeat everything but with radius 0.9 in place of 0.8 when defining the distributions P_2 and P'_2 . Then for the APF₀s, the proportion of wrong assignments has a mean of 23.2% and a standard deviation of 2.9%, and for the APF₁s, a mean of 5.7% and a standard deviation of 1.9%. Similar to Example 7, the error is lowest when $k = 1$ and this is due to the largest lifetime of a loop.

Acknowledgment

Supported by the "Centre for Stochastic Geometry and Advanced Bioimaging", funded by grant 8721 from the Villum Foundation. Helpful discussions with Lisbeth Fajstrup on persistence homology is acknowledged. In connection to the brain artery trees dataset we thank James Stephen Marron and Sean Skwerer for helpful discussions and the CASILab at The University of North Carolina at Chapel Hill for providing the data distributed by the MIDAS Data Server at Kitware, Inc.

Appendix A

The proof of Theorem 4.1 follows along similar lines as in Chazal *et al.* (2013) as soon as we have verified Lemma A.2 below. Note that the proof of Lemma A.2 is not covered by the approach in Chazal *et al.* (2013).

We first need to recall the following definition, where \mathcal{B}_T denotes the topological space of bounded real valued Borel functions defined on $[0, T]$ and its topology is induced by the uniform norm.

Definition A.1. A sequence $\{X_r\}_{r=1,2,\dots}$ of random elements in \mathcal{B}_T converges in distribution to a random element X in \mathcal{B}_T if for any bounded continuous function $f : \mathcal{B}_T \mapsto \mathbb{R}$, $\text{Ef}(X_r)$ converges to $\text{Ef}(X)$ as $r \rightarrow \infty$.

Lemma A.2. Let the situation be as in Section 4.2. As $r \rightarrow \infty$, $\sqrt{r} (\bar{A}_r - \mu)$ converges in distribution towards a zero-mean Gaussian process on $[0, T]$ with covariance function $c(m, m') = \text{Cov}(A_1(m), A_1(m'))$, $m, m' \in [0, T]$.

Proof. We need some notation and to recall some concepts of empirical process theory. For $D \in \mathcal{D}_T^{k, n_{\max}}$, denote A_D the APF $_k$ of D . Let $\mathcal{F} = \{f_m : 0 \leq m \leq T\}$ be the class of functions $f_m : \mathcal{D}_T^{k, n_{\max}} \mapsto [0, \infty)$ given by $f_m(D) = A_D(m)$. Denote $\|\cdot\|$ the L^2 norm on \mathcal{F} with respect to the distribution of D_1 , i.e. $\|f_m(\cdot)\|^2 = \mathbb{E}\{A_{D_1}(m)^2\}$. For $u, v \in \mathcal{F}$, the bracket $[u, v]$ is the set of all functions $f \in \mathcal{F}$ with $u \leq f \leq v$. For any $\epsilon > 0$, $N_{[]}(\epsilon, \mathcal{F}, \|\cdot\|)$ is the smallest integer $J \geq 1$ such that $\mathcal{F} \subset \cup_{j=1}^J [u_j, v_j]$ for some functions u_1, \dots, u_J and v_1, \dots, v_J in \mathcal{F} with $\|v_j - u_j\| \leq \epsilon$ for $j = 1, \dots, J$. We show below that $N_{[]}(\epsilon, \mathcal{F}, \|\cdot\|)$ is finite. Note that the convergence in Lemma A.2 means that \mathcal{F} is a so-called Donsker class with respect to the distribution of D_1 , see e.g. van der Vaart and Wellner (1996).

For any sequence $-\infty = t_1 < \dots < t_J = \infty$ with $J \geq 2$, for $j = 1, \dots, J-1$, and for $D = \{(m_1, l_1, c_1), \dots, (m_n, l_n, c_n)\} \in \mathcal{D}_T^{k, n_{\max}}$, let $u_j(D) = \sum_{i=1}^n c_i l_i 1(m_i \leq t_j)$ and $v_j(D) = \sum_{i=1}^n c_i l_i 1(m_i < t_{j+1})$ (if $n = 0$, then D is empty and we set $u_j(D) = v_j(D) = 0$). Then, for any $m \in [0, T]$, there exists a $j = j(m)$ such that $u_j(D) \leq f_m(D) \leq v_j(D)$, i.e. $f_m(D) \in [u_j, v_j]$. Consequently, $\mathcal{F} \subset \cup_{j=1}^{J-1} [u_j, v_j]$.

We prove now that for any $\epsilon \in (0, 1)$, the sequence $\{t_j\}_{1 \leq j \leq J}$ can be chosen such that for $j = 1, \dots, J-1$, we have $\|v_j - u_j\| \leq \epsilon$. Write $D_1 = \{(M_1, L_1, C_1), \dots, (M_N, L_N, C_N)\}$, where N is random and should not to be confused with N in Sections 2.1 and 3.1 (if $N = 0$, then D_1 is empty). Let $n \in \{1, \dots, n_{\max}\}$ and conditioned on $N = n$, let I be uniformly selected from $\{1, \dots, n\}$. Then

$$\begin{aligned} \mathbb{E} \left\{ (v_j(D_1) - u_j(D_1))^2 1(N = n) \right\} &= n^2 \mathbb{E} \left\{ 1(N = n) \frac{1}{n} \sum_{i=1}^n C_i L_i 1(M_i \in (t_j, t_{j+1})) \right\}^2 \\ &\leq T^2 n_{\max}^4 \mathbb{E} \left\{ 1(N = n) 1(M_I \in (t_j, t_{j+1})) \right\}^2 \\ &\leq T^2 n_{\max}^4 \mathbb{P}(M_I \in (t_j, t_{j+1}) | N = n), \end{aligned}$$

as $n \leq n_{\max}$, $C_i \leq n_{\max}$, and $L_i \leq T$. Further,

$$\mathbb{E} \left\{ (v_j(D_1) - u_j(D_1))^2 1(N = 0) \right\} = 0.$$

Hence

$$\begin{aligned} \mathbb{E} \left\{ v_j(D_1) - u_j(D_1) \right\}^2 &= \sum_{n=0}^{n_{\max}} \mathbb{E} \left\{ (v_j(D_1) - u_j(D_1))^2 1(N = n) \right\} \\ &\leq T^2 n_{\max}^5 \max_{n=1, \dots, n_{\max}} \mathbb{P}(M_I \in (t_j, t_{j+1}) | N = n). \end{aligned} \quad (14)$$

Moreover, by Lemma A.3 below, there exists a finite sequence $\{t_{n,j}\}_{1 \leq j \leq J_n}$ such that $\mathbb{P}(M_I \in (t_{n,j}, t_{n,j+1}) | N = n) \leq \epsilon^2 / (T^2 n_{\max}^5)$ and $J_n \leq 2 + T^2 n_{\max}^5 / \epsilon^2$. Thus, by choosing

$$\{t_j\}_{1 \leq j \leq J} = \bigcup_{n=1, \dots, n_{\max}} \{t_{n,j}\}_{1 \leq j \leq J_n},$$

we have $J \leq 2n_{\max} + T^2 n_{\max}^6 / \epsilon^2$ and

$$\max_{n=1, \dots, n_{\max}} \mathbb{P}(M_I \in (t_j, t_{j+1}) | N = n) \leq \frac{\epsilon^2}{T^2 n_{\max}^5}.$$

Hence by (14), $\|v_j - u_j\| \leq \epsilon$, and so by definition, $N_{\square}(\epsilon, \mathcal{F}, \|\cdot\|) \leq 2n_{\max} + T^2 n_{\max}^6 / \epsilon^2$. Therefore

$$\int_0^1 \sqrt{\log \left(N_{\square}(\epsilon, \mathcal{F}, \|\cdot\|) \right)} d\epsilon \leq \int_0^1 \sqrt{\log (2n_{\max} + T^2 n_{\max}^6 / \epsilon^2)} d\epsilon < \infty,$$

and so \mathcal{F} is by Theorem 19.5 in van der Vaart (2000) a so-called Donsker class. \square

Lemma A.3. *Let X be a positive random variable. For any $\epsilon \in (0, 1)$, there exists a finite sequence $-\infty = t_1 < \dots < t_J = \infty$ such that $J \leq 2 + 1/\epsilon$ and for $j = 1, \dots, J-1$,*

$$\mathbb{P}(X \in (t_j, t_{j+1})) \leq \epsilon.$$

Proof. Denote by F the cumulative distribution function of X , by $F(t-)$ the left-sided limit of F at $t \in \mathbb{R}$, and by F^{-1} the generalised inverse of F , i.e. $F^{-1}(y) = \inf\{x \in$

$\mathbb{R} : F(x) \geq y\}$ for $y \in \mathbb{R}$. We verify the lemma with $J = 2 + \lfloor 1/\epsilon \rfloor$, $t_J = \infty$, and $t_j = F^{-1}((j-1)\epsilon)$ for $j = 1, \dots, J-1$. Then, for $j = 1, \dots, J-2$,

$$P(X \in (t_j, t_{j+1})) = F(F^{-1}(j\epsilon)) - F(F^{-1}((j-1)\epsilon)) \leq j\epsilon - (j-1)\epsilon = \epsilon.$$

Finally,

$$P(X \in (t_{J-1}, t_J)) = P(X > F^{-1}((J-2)\epsilon)) = 1 - F(F^{-1}((J-2)\epsilon)) \leq 1 - \lfloor 1/\epsilon \rfloor \epsilon < \epsilon.$$

□

References

- Baddeley, A., Rubak, E. & Turner, R. (2015). *Spatial Point Patterns: Methodology and Applications with R*. Chapman and Hall/CRC Press.
- Baddeley, A. J. & Silverman, B. W. (1984). A cautionary example on the use of second-order methods for analyzing point patterns. *Biometrics* **40**, 1089–1093.
- Bendich, P., Marron, J., Miller, E., Pieloch, A. & Skwerer, S. (2016). Persistent homology analysis of brain artery trees. *The Annals of Applied Statistics* **10**, 198–218.
- Biscio, C. A. N. & Lavancier, F. (2016). Quantifying repulsiveness of determinantal point processes. *Bernoulli* **22**, 2001–2028.
- Bottou, L. & Bengio, Y. (1995). Convergence properties of the k-means algorithms. In: *Advances in Neural Information Processing Systems*, volume 7, MIT Press, 585–592.
- Bubenik, P. (2015). Statistical topological data analysis using persistence landscapes. *Journal of Machine Learning Research* **16**, 77–102.
- Chazal, F., Cohen-Steiner, D., Guibas, L. J., Mémoi, F. & Oudot, S. Y. (2009). Gromov-Hausdorff stable signatures for shapes using persistence. *Computer Graphics Forum* **28**, 1393–1403.
- Chazal, F., Fasy, B., Lecci, F., Rinaldo, A., Singh, A. & Wasserman, L. (2013). On the bootstrap for persistence diagrams and landscapes. *Modeling and Analysis of Information Systems* **20**, 111–120.
- Chazal, F., Fasy, B. T., Lecci, F., Michel, B., Rinaldo, A. & Wasserman, L. (2014). Robust topological inference: Distance to a measure and kernel distance. Available on arXiv:1412.7197.
- Chen, Y.-C., Wang, D., Rinaldo, A. & Wasserman, L. (2015). Statistical analysis of persistence intensity functions. Available on arXiv: 1510.02502.
- Daley, D. J. & Vere-Jones, D. (2003). *An Introduction to the Theory of Point Processes. Volume I: Elementary Theory and Methods*. Springer-Verlag, New York, 2nd edition.

- Edelsbrunner, H. & Harer, J. L. (2010). *Computational Topology*. American Mathematical Society, Providence, RI.
- Fasy, B., Lecci, F., Rinaldo, A., Wasserman, L., Balakrishnan, S. & Singh, A. (2014). Confidence sets for persistence diagrams. *The Annals of Statistics* **42**, 2301–2339.
- Hartigan, J. A. & Wong, M. A. (1979). Algorithm AS 136: A k-means clustering algorithm. *Journal of the Royal Statistical Society: Series C (Applied Statistics)* **28**, 100–108.
- Jacques, J. & Preda, C. (2014). Functional data clustering: a survey. *Advances in Data Analysis and Classification* **8**, 231–255.
- Lavancier, F., Møller, J. & Rubak, E. (2015). Determinantal point process models and statistical inference. *Journal of the Royal Statistical Society: Series B (Statistical Methodology)* **77**, 853–877.
- López-Pintado, S. & Romo, J. (2009). On the concept of depth for functional data. *Journal of the American Statistical Association* **104**, 718–734.
- López-Pintado, S., Romo, J. & Torrente, A. (2010). Robust depth-based tools for the analysis of gene expression data. *Biostatistics* **11**, 254–264.
- MacPherson, R. & Schweinhart, B. (2012). Measuring shape with topology. *Journal of Mathematical Physics* **53**, 073516.
- Matérn, B. (1986). *Spatial Variation*. Lecture Notes in Statistics 36, Springer-Verlag, Berlin.
- Møller, J. & Waagepetersen, R. P. (2004). *Statistical Inference and Simulation for Spatial Point Processes*. Chapman and Hall/CRC, Boca Raton.
- Møller, J. & Waagepetersen, R. P. (2016). Some recent developments in statistics for spatial point patterns. *Annual Review of Statistics and Its Application* To appear.
- Mrkvička, T., Myllymäki, M. & Hahn, U. (2016). Multiple monte carlo testing, with applications in spatial point processes. *Statistics and Computing* , 1–17.
- Myllymäki, M., Mrkvička, T., Grabarnik, P., Seijo, H. & Hahn, U. (2016). Global envelope tests for spatial processes. *Journal of the Royal Statistical Society: Series B (Statistical Methodology)* Available on arXiv:1307.0239.
- Præstgaard, J. T. (1995). Permutation and bootstrap Kolmogorov-Smirnov tests for the equality of two distributions. *Scandinavian Journal of Statistics* **22**, 305–322.
- Robins, V. & Turner, K. (2016). Principal component analysis of persistent homology rank functions with case studies of spatial point patterns, sphere packing and colloids. *Physica D: Nonlinear Phenomena* **334**, 99–117.

- Sun, Y. & Genton, M. G. (2011). Functional boxplots. *Journal of Computational and Graphical Statistics* **20**, 316–334.
- van der Vaart, A. W. (2000). *Asymptotic Statistics*. Cambridge University Press, Cambridge.
- van der Vaart, A. W. & Wellner, J. A. (1996). *Weak Convergence and Empirical Processes*. Springer Series in Statistics, Springer-Verlag, New York.